

# The age of the hominin fossils from Jebel Irhoud, Morocco, and the origins of the Middle Stone Age

Daniel Richter<sup>1,2,3</sup>, Rainer Grün<sup>4,5</sup>, Renaud Joannes-Boyau<sup>4,6</sup>, Teresa E. Steele<sup>1,7</sup>, Fethi Amani<sup>8</sup>, Mathieu Rué<sup>9,10</sup>, Paul Fernandes<sup>9,11</sup>, Jean-Paul Raynal<sup>1,11</sup>, Denis Geraads<sup>1,12</sup>, Abdelouahed Ben-Ncer<sup>8</sup>, Jean-Jacques Hublin<sup>1,13</sup> & Shannon P. McPherron<sup>1</sup>

The timing and location of the emergence of our species and of associated behavioural changes are crucial for our understanding of human evolution. The earliest fossil attributed to a modern form of *Homo sapiens* comes from eastern Africa and is approximately 195 thousand years old<sup>1,2</sup>, therefore the emergence of modern human biology is commonly placed at around 200 thousand years ago<sup>3,4</sup>. The earliest Middle Stone Age assemblages come from eastern and southern Africa but date much earlier<sup>5–7</sup>. Here we report the ages, determined by thermoluminescence dating, of fire-heated flint artefacts obtained from new excavations at the Middle Stone Age site of Jebel Irhoud, Morocco, which are directly associated with newly discovered remains of *H. sapiens*<sup>8</sup>. A weighted average age places these Middle Stone Age artefacts and fossils at  $315 \pm 34$  thousand years ago. Support is obtained through the recalculated uranium series with electron spin resonance date of  $286 \pm 32$  thousand years ago for a tooth from the Irhoud 3 hominin mandible. These ages are

also consistent with the faunal and microfaunal<sup>9</sup> assemblages and almost double the previous age estimates for the lower part of the deposits<sup>10,11</sup>. The north African site of Jebel Irhoud contains one of the earliest directly dated Middle Stone Age assemblages, and its associated human remains are the oldest reported for *H. sapiens*. The emergence of our species and of the Middle Stone Age appear to be close in time, and these data suggest a larger scale, potentially pan-African, origin for both.

Jebel Irhoud (Irhoud), Morocco (Fig. 1 and Extended Data Fig. 1), contains stratified archaeological deposits (Fig. 2) best known for yielding abundant late Pleistocene hominin remains associated with a Levallois-based Middle Stone Age stone-tool assemblage<sup>8,12</sup> (Fig. 3 and Extended Data Figs 4–6). Taxonomically these fossils have generally been considered to be primitive forms of *H. sapiens*<sup>13</sup>, but they have been dated to a relatively recent age<sup>11</sup>. However, the uncertain find location of the key fossils has limited the accuracy of their age estimates.



**Figure 1 | Excavation site and hominin fossils.**

**a**, South view of the site with the inset showing the location of Irhoud in northwest Africa. The remaining deposits are located in what was a tunnel-like karstic feature dipping to the east that was later fully exposed (at least in part to the left) by quarrying-related activities. The remaining *in situ* sediments are to the right of the blue tarp. The red circle indicates where the hominin remains shown in **b** and **c** were found (photo taken after the hominins were removed; photo is a composite image with some distortion noticeable left and right). **b**, View showing the partial skull (Irhoud 1678/Irhoud 10) in the centre foreground (white arrow) and the femur (Irhoud 2252/Irhoud 13) in the centre background (yellow arrow). The back centre and left is the cliff face. The archaeological material is resting on a large boulder (the 10-cm scale bar is at the contact). **c**, Plan view of **b**, but after additional excavation. The partial skull (white arrow) and femur (yellow arrow) are still present. The mandible (Irhoud 4765/Irhoud 11) is wrapped around the upper corner of the pyramid-shaped rock. A portion of the right tooth row is clearly visible (red arrow). A smaller portion of the left tooth row is also visible. The photograph was taken after the area (including the skull and femur) had been covered with glue before moulding (see Supplementary Information). Some glue has also been applied to the mandible to stabilize it before removal.

<sup>1</sup>Department of Human Evolution, Max Planck Institute for Evolutionary Anthropology, Deutscher Platz 6, Leipzig 04103, Germany. <sup>2</sup>Institute of Ecology, Subject Area Landscape Change, Leuphana University Lüneburg, Scharnhorststrasse 1, 21335 Lüneburg, Germany. <sup>3</sup>Freiberg Instruments GmbH, Delfterstrasse 6, 09599 Freiberg, Germany. <sup>4</sup>Research School of Earth Sciences, The Australian National University, Canberra, Australian Capital Territory 0200, Australia. <sup>5</sup>Australian Research Centre for Human Evolution, Environmental Futures Research Institute, Griffith University, Nathan, Queensland 4111, Australia. <sup>6</sup>Southern Cross GeoScience, Southern Cross University, Military Road, Lismore, New South Wales 2480, Australia. <sup>7</sup>Department of Anthropology, University of California, Davis, One Shields Avenue, Davis California, USA. <sup>8</sup>Institut National des Sciences de L'Archéologie et du Patrimoine, Ministère de la Culture et de la Communication, Hay Riad, Madinat Al Ifrane, Angle rues 5 et 7, BP 6828, Rabat, Morocco. <sup>9</sup>Paléotime, 6173 Rue Jean Séraphin Achard Picard, 38250 Villard-de-Lans, France. <sup>10</sup>Archéologie des Sociétés Méditerranéennes, (ASM, UMR 5140 CNRS), Université Paul-Valéry, Montpellier 3, MCC, Route de Mende, 34199 Montpellier cedex 5, France. <sup>11</sup>De la Préhistoire à l'Actuel : Culture, Environnement, Anthropologie (PACEA, UMR 5199 CNRS), Université de Bordeaux, MCC, Bâtiment B18, Allée Geoffroy Saint-Hilaire, CS 50023, 33615, Pessac, France. <sup>12</sup>Centre de Recherches sur la Paléobiodiversité et les Paléoenvironnements (CR2P, UMR 7207 CNRS), Sorbonne Universités, MNHN, UPMC, CP 38, 8 Rue Buffon, 75231 Paris cedex 05 France. <sup>13</sup>Chaire Internationale de Paléanthropologie, Collège de France, Paris, France.

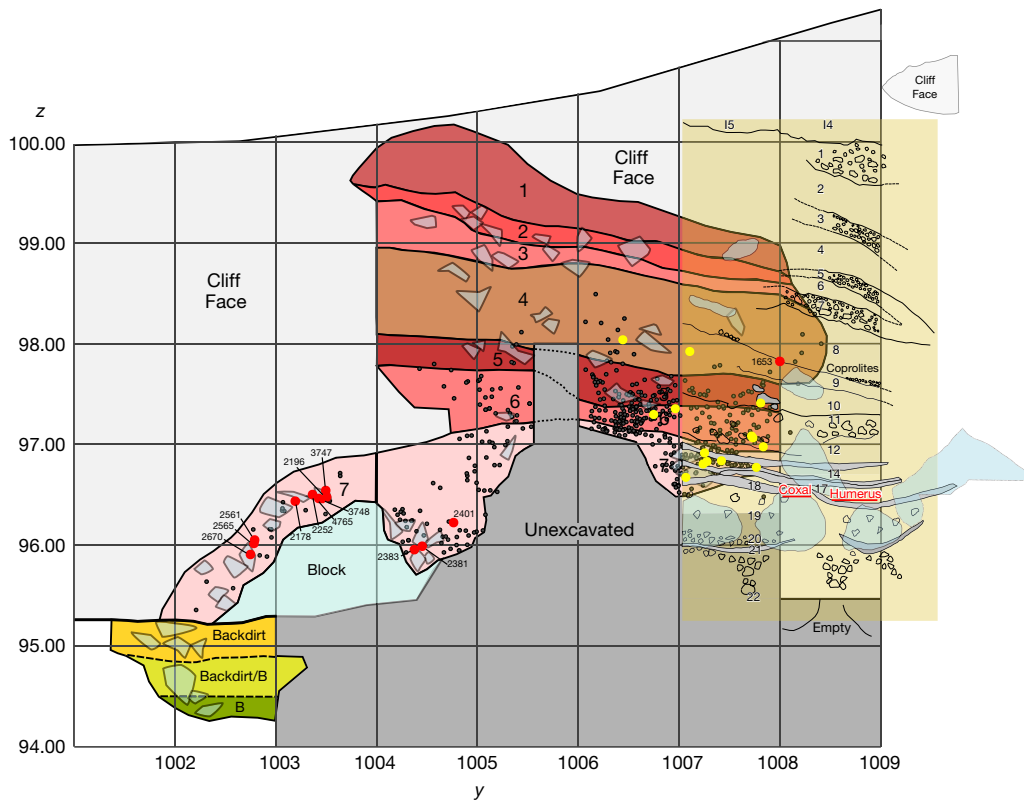


**Figure 2 | South view of the profile (in m) showing the main stratigraphic units of our excavations correlated with the previous stratigraphic profile.** The layer designations on the right (1–22) are based on the previous publication (see ref. 12). The designations in the centre and on the left are our designations (numbers and letters in the coloured layers). A strict correspondence between the two is not possible; however, it is clear that the hominins recovered previously<sup>12</sup> (the coxal and humerus noted in red) correspond to our layer 7. The correlation of the two stratigraphic profiles is based on field observations including finding nails

from the previous excavations<sup>12</sup>. Layer B is stratigraphically unconnected to the rest of the sequence. The viewing angle of this section roughly corresponds to the view in Extended Data Fig. 1. The clearly visible (in the preserved profile) continuation of the layers is indicated as dotted lines for the as yet unexcavated sediment. Our fossil finds are indicated with red dots. The location of the coxal is estimated based on descriptions in ref. 15. The location of the humerus comes from ref. 12. Heated flints used for thermoluminescence dating are indicated with yellow dots. Stone tools are indicated with smaller grey dots.

Electron spin resonance (ESR) dating of three mammal teeth from the deposit immediately overlying a partial humerus, the only hominin fossil at the time with a precisely documented find location, has resulted in an age range of 190 to 90 thousand years (ka)<sup>11</sup>, while a coupled U-series(US)/ESR<sup>14</sup> age for a human tooth fragment of  $160 \pm 16$  kyr has been suggested<sup>10</sup>. All these results were, however, based on single estimates of the external  $\gamma$ -doses obtained from sediment samples of uncertain stratigraphic context.

New excavations were initiated in 2004 on the complete, intact section remaining from the late 1960s excavations<sup>12</sup> (Fig. 1b). This section rests against the cave wall and atop large blocks that are likely to represent a roof fall. On the basis of the limited documentation that is available of the geomorphology before the cave was opened by recent blasting, the remaining deposits appear to have been located within the cave. The deposits are poorly stratified and poorly sorted, contain occasional gravel lenses, and were formed mainly through processes of debris flow and run-off, including material from the exterior. There were no major post-depositional disturbances which could have caused mixing or important disturbances for the dosimetry (Extended Data Figs 2, 3 and Supplementary Information). Within this deposit, 7 layers are distinguished and well-correlated with the 22 layers that have been previously reported (Fig. 2). Layers 1–3, representing the upper approximately 75 cm of the remaining deposits, contain very little archaeological material. Layers 4–6 form a thick deposit (175 cm) of relatively undifferentiated, unsorted, compacted sediments with varying sized clasts and include some archaeological material. Layer 7 is similar, but contains pockets of cemented sediments and the highest density of archaeological finds. We noted in layer 7, as well as at the

contact between layers 5 and 6 in the unexcavated profile, several spatially constrained centimetre-thick accumulations consisting at least partially of charcoal (see Supplementary Information) that are tentatively interpreted as features related to combustion. These features are consistent with limited post-depositional disturbance and, along with the occurrence of heated lithics throughout the sequence, they attest to the presence of fire at Jebel Irhoud.

The stone tools and most of the faunal remains are concentrated in the lower portion of the deposit, especially layer 7. Additionally, except for one tooth (Irhoud-1653), all the newly discovered hominins<sup>8</sup> come from layer 7 (Fig. 2). Most were excavated from a wedge of layer 7 sediment extending east from the main sediment block along the bedrock face (Fig. 1) within an area of approximately  $40 \times 40$  cm. Among the previously discovered fossils, the Irhoud 4 humerus<sup>12</sup> and Irhoud 5 coxal<sup>15</sup> can also be securely correlated to layer 7 (Fig. 2).

The fauna are dominated by remains of gazelle (*Gazella* sp.), but Equidae (zebras) and Alcelaphini (wildebeest and hartebeest) remains are also present (Supplementary Information). The faunal assemblage preserves a diversity of carnivores; leopards (*Panthera pardus*) are most common, but there are also remains of lions (*Panthera leo*) and smaller cats. While carnivore remains and hyena coprolites are consistently found in low abundance throughout the sequence, there is only a single carnivore-chewed bone (a gazelle rib from layer 6). A primarily anthropogenic origin for the fauna is confirmed by the majority of long bones exhibiting green or fresh breaks (at least 61% in layer 4, 69% in layer 5, 54% in layer 6 and 60% in layer 7), by probable stone-tool cut-marks on gazelle bones from layers 4 (one rib), 6 (one rib) and 7 (one distal humerus and one fragment of a long bone), by a few

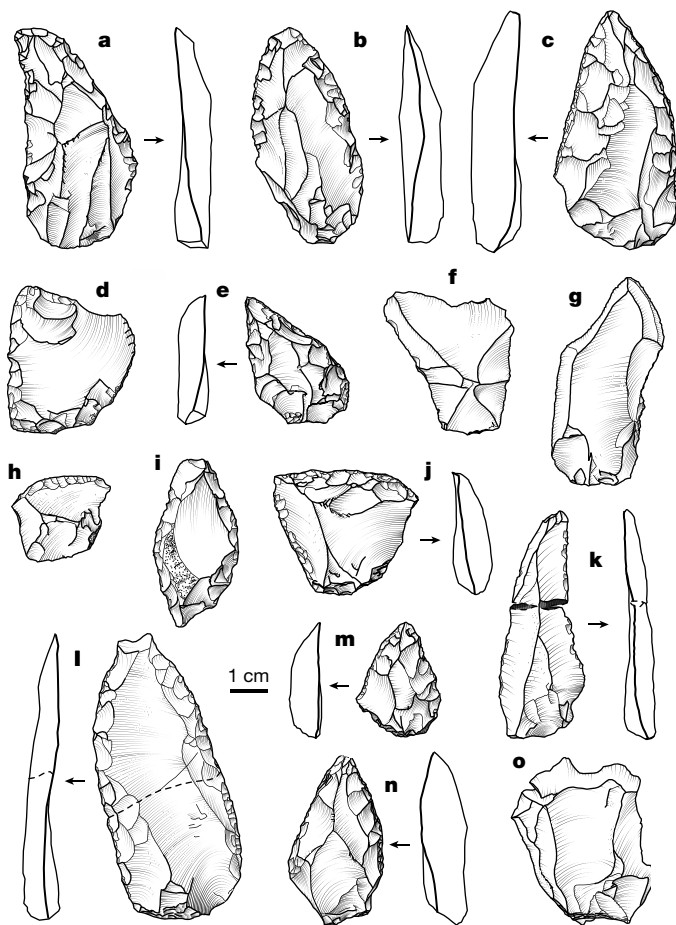


**Figure 3 | Flint artefacts from layers 6 and 7.** a–e, Convergent scrapers (layer 6). f, g, Levallois flakes (layer 6). h, Transverse scraper (layer 6). i, Limace (layer 6). j, Déjété scraper (layer 7). k, Levallois flake (layer 7). l, Convergent scraper (layer 7). m, Convergent scraper (layer 7). n, Unifacial point (layer 7). o, Levallois flake (layer 7). Outlines represent profile views.

percussion notches consistent with marrow extraction, and by the relatively high abundance of burnt bones (5% in layer 4, 25% in layer 5, 19% in layer 6 and 24% in layer 7). An analysis of the rodent remains from the sequence suggests a maximum age of marine isotope stage (MIS) 10 (374–337 kyr)<sup>16</sup>, with strong indications that the sequence is not much younger than this<sup>9</sup>.

The lithics of these new Middle Stone Age assemblages are consistent with previous descriptions of the Jebel Irhoud material<sup>12</sup> and are dominated by Levallois technology with a high proportion of retouched tools, especially pointed forms (Fig. 3, Extended Data Figs 4–6, Extended Data Table 1 and Supplementary Information). No characteristic Acheulean or Aterian elements are present. There is little evidence of post-depositional alteration and taphonomic bias in the artefact assemblage: 56% of the lithics show no edge damage and 76% of the blanks are complete. There is an underrepresentation of lithic material from the screens (5–25 mm), which could indicate selective water transport of fine materials. Given the low frequency of cores and of shatter (see Extended Data Table 1), it is more likely indicative of a lithic production system emphasizing blank and/or tool importation with limited on-site production using local raw materials.

Although the excavated artefact assemblage is relatively small ( $n = 320$  artefacts larger than 2.5 cm), the high percentage of visibly (37%) heated flint artefacts allows thermoluminescence dating of the archaeological assemblage and associated human remains. External  $\gamma$ -dose-rates for each layer were measured<sup>17</sup> *in situ* before excavation with 47  $\alpha$ - $\text{Al}_2\text{O}_3$ :C dosimeters. The  $\gamma$ -dose-rates within each layer have large dispersions of 8 to 14% (1 standard deviation ( $\sigma$ )) (Extended

**Table 1 | Individual thermoluminescence and thermoluminescence context ages ( $1\sigma$ ) of heated flint artefacts with percentage contribution of the stable internal and external  $\gamma$ -dose-rates to the total dose-rate (stable cosmic dose contribution<sup>31</sup> is not given)**

EVA-LUM (Lab. number)	Layer	$\dot{D}$ -external (% total $\dot{D}$ )	$\dot{D}$ - $\gamma$ -external (% total $\dot{D}$ )	Age (ka)	Statistical uncertainty (ka)	Total uncertainty (ka)
07/15	4	21	72	274	20	36
07/16	4	25	69	374	35	52
07/17	5	55	41	292	18	27
07/18	5	22	72	309	12	35
07/19	6	26	68	240	24	35
07/21	6	37	58	290	19	32
07/25	6	30	64	322	13	34
08/03	6	22	72	307	26	42
Layer 6 weighted average context age				302	16	32
07/28*	7A	42	53	378	20	30
08/05	7A	25	69	295	9	32
08/06	7A	20	74	310	15	38
08/07	7A	32	63	328	10	33
08/08	7A	22	72	332	16	41
08/12	7B	36	59	329	31	44
Layer 7 weighted average context age				315	11	34

\*Weighted average of 2 subsamples.

Data Table 2), demonstrating the inhomogeneity of the sediments. Therefore, layer  $\gamma$ -dose-rate averages plus the dating of several objects per layer are required for dosimetric dating in order to obtain reliable results<sup>18,19</sup>. This approach is possible with the new excavations, where the stratigraphic provenience of the samples is known, unlike previous dosimetric dating attempts<sup>10,11</sup> with ESR. High-purity germanium (HpGe)  $\gamma$ -ray spectrometry (Extended Data Table 2) shows that the U and Th radioactive decay chain activities are consistent with present day secular equilibrium, which leads us to assume that the external  $\gamma$ -dose-rates have been constant over the entire burial time. The palaeodoses were determined with a multiple aliquot additive regeneration slide approach<sup>20–22</sup> (Extended Data Fig. 7).

A total of 14 ages, as determined by thermoluminescence dating, were obtained (Table 1 and Extended Data Table 2). The apparent ages range from  $240 \pm 35$  ka to  $378 \pm 30$  ka (Table 1) for the entire stratigraphy with dispersions of age results for the individual layers similar to those observed for the  $\gamma$ -dose-rates. Such a wide age range is typical<sup>18,23</sup> when individual artefact ages are based on layer averaged  $\gamma$ -dose-rates in such heterogeneous or lumpy<sup>19</sup> sediments. We are assuming that the ages and associated individual dose-rates exhibit a quasi-random dispersion around the mean  $\gamma$ -dose-rate<sup>18,19,23</sup>. Sample sizes are sufficient<sup>23</sup> for calculating weighted average ages for layers 6 and 7 and yield ages of  $302 \pm 32$  ka and  $315 \pm 34$  ka, respectively.

The published ESR age of the Irhoud 3 fossil<sup>10</sup> was based on an external dose-rate measured on a small sediment sample of imprecise stratigraphic context. Assuming an origin from a layer-7-like deposit, it can be recalculated using the *in situ*  $\gamma$ -dosimetry that is now available (Extended Data Table 2) and with additional recent insights into the ESR dose estimation of solid enamel fragments<sup>24</sup>. The combined US/ESR dating system<sup>14</sup> assumes a continuous U-uptake based on a single-parameter ( $p$  value) diffusion equation. Using this system, US/ESR analysis results in an age of  $281 + 37/-29$  ka with a  $p$  value of  $-0.27$ . The closed system US/ESR (CSUS/ESR)<sup>25</sup>, which assumes a fast U-uptake at the time before present corresponding to a closed U system, yields an age estimate of  $286 \pm 32$  ka. The age range of both

models, around 350–220 ka at  $2\sigma$ , provides an error envelope that encompasses most possible scenarios of how the uranium diffused into the dental tissue.

The thermoluminescence data suggest that the Middle Stone Age industry from layer 7 has a 95% probability ( $2\sigma$ ) of dating to 383–247 ka, an age that is also in agreement with the fauna and microfauna<sup>9</sup> of the site. The stratigraphy shows that the dated artefacts and the hominin remains originate from the same geological layer, and thus the age range obtained for the heated flints can be used to estimate the age of the hominin fossils. Additionally, the direct US/ESR date for the Irhoud 3 specimen is consistent with the thermoluminescence average ages for layers 6 and 7.

Our ages for Jebel Irhoud overlap with those reported for the Florisbad partial cranium<sup>26</sup>, suggesting that the hominins from Irhoud<sup>8</sup> and Florisbad represent the earliest known representatives of the *H. sapiens* clade. The ages for the heated artefacts from layer 7 are probably older than the sediments containing a Levallois-based Middle Stone Age assemblage in the Maghreb, which were dated using optically stimulated luminescence (OSL) to  $254 \pm 17$  ka (ref. 27). In east Africa, the Middle Stone Age at ETH-72-8B (Gademotta, Ethiopia) occurs before  $275 \pm 6$  ka (ref. 6) and in the Kapthurin Formation (Baringo, Kenya) before  $284 \pm 12$  ka (ref. 5) (calculated to  $282 \pm 20$  ka)<sup>6</sup> based on <sup>40</sup>Ar/<sup>39</sup>Ar-dating of overlying tuffs. In southern Africa, a redeposited Middle Stone Age assemblage at Kathu Pan layer 3 dates to before  $291 \pm 45$  ka (ref. 7) based on OSL ages. Therefore by approximately 300 ka or soon after MIS 9 (337–300 ka)<sup>16</sup>, Levallois technology was distributed across a large part of Africa and Eurasia<sup>28</sup> and was in Africa associated with the earliest dated occurrences of *H. sapiens*. The Saharan desert was greatly reduced during a series of Middle Pleistocene ‘green Sahara’ episodes, with an especially marked but short period around 330 ka (ref. 29). This would have allowed ecological continuity between north Africa and sub-Saharan Africa. Biological continuity between east and northwest Africa is also supported by strong faunal similarities, especially for the Middle Pleistocene, suggesting at least frequent communication between these regions<sup>30</sup> (and see Supplementary Information). Therefore, whether the Jebel Irhoud data suggest an even earlier origin for the Middle Stone Age that was directly associated with the emergence of *H. sapiens* and followed by a relatively rapid dispersal or whether there were multiple, regionally specific, but related origins<sup>28</sup> is as yet unclear. Minimally, these behavioural data, along with the associated fossil evidence, suggest a complex pan-African process before or around 300 ka, a period for which we still have relatively few data points, and we caution against favouring one region over another in constructing models to account for these changes in human behaviour and biology.

**Online Content** Methods, along with any additional Extended Data display items and Source Data, are available in the online version of the paper; references unique to these sections appear only in the online paper.

**Received 4 May 2016; accepted 5 April 2017.**

- McDougall, I., Brown, F. H. & Fleagle, J. G. Sapropels and the age of hominins Omo I and II, Kibish, Ethiopia. *J. Hum. Evol.* **55**, 409–420 (2008).
- Brown, F. H., McDougall, I. & Fleagle, J. G. Correlation of the KHS Tuff of the Kibish Formation to volcanic ash layers at other sites, and the age of early *Homo sapiens* (Omo I and Omo II). *J. Hum. Evol.* **63**, 577–585 (2012).
- Scheinfeldt, L. B., Soi, S. & Tishkoff, S. A. Colloquium paper: working toward a synthesis of archaeological, linguistic, and genetic data for inferring African population history. *Proc. Natl Acad. Sci. USA* **107**, 8931–8938 (2010).
- Gronau, I., Hubisz, M. J., Gulko, B., Danko, C. G. & Siepel, A. Bayesian inference of ancient human demography from individual genome sequences. *Nat. Genet.* **43**, 1031–1034 (2011).
- Deino, A. L. & McBrearty, S. <sup>40</sup>Ar/<sup>39</sup>Ar dating of the Kapthurin Formation, Baringo, Kenya. *J. Hum. Evol.* **42**, 185–210 (2002).
- Sahle, Y., Morgan, L. E., Braun, D. R., Atnafu, B. & Hutchings, W. K. Chronological and behavioral contexts of the earliest Middle Stone Age in the Gademotta Formation, Main Ethiopian Rift. *Quat. Int.* **331**, 6–19 (2014).
- Porat, N. et al. New radiometric ages for the Fauresmith industry from Kathu Pan, southern Africa: implications for the Earlier to Middle Stone Age transition. *J. Archaeol. Sci.* **37**, 269–283 (2010).

- Hublin, J.-J. et al. New fossils from Jebel Irhoud, Morocco and the pan-African origin of *Homo sapiens*. *Nature* <http://dx.doi.org/10.1038/nature22336> (2017).
- Geraads, D. et al. The rodents from the late Middle Pleistocene hominid-bearing site of J'bel Irhoud, Morocco, and their chronological and paleoenvironmental implications. *Quat. Res.* **80**, 552–561 (2013).
- Smith, T. M. et al. Earliest evidence of modern human life history in north African early *Homo sapiens*. *Proc. Natl Acad. Sci. USA* **104**, 6128–6133 (2007).
- Grün, R. & Stringer, C. B. Electron spin resonance dating and the evolution of modern humans. *Archaeometry* **33**, 153–199 (1991).
- Hublin, J.-J., Tillier, A. M. & Tixier, J. L'humérus d'enfant moustérien (Homo 4) du Djebel Irhoud (Maroc) dans son contexte archéologique. *Bull. Mem. Soc. Anthropol. Paris* **4**, 115–141 (1987).
- Hublin, J.-J. Recent human evolution in northwestern Africa. *Phil. Trans. R. Soc. Lond. B* **337**, 185–191 (1992).
- Grün, R., Schwarcz, H. P. & Chadam, J. ESR dating of tooth enamel: Coupled correction for U-uptake and U-series disequilibrium. *Int. J. Rad. Appl. Instrum. D* **14**, 237–241 (1988).
- Tixier, J., Brugal, J., Tillier, A. M., Bruzek, J. & Hublin, J. Irhoud 5, un fragment d'os coxal non-adulte des niveaux moustériens marocains. *Actes J. Natl. Archéol. Patrim. Maroc* 149–153 (2001).
- Lisiecki, L. E. & Raymo, M. E. A Pliocene–Pleistocene stack of 57 globally distributed benthic  $\delta^{18}\text{O}$  records. *Paleoceanography* **20**, PA1003 (2005).
- Richter, D., Dombrowski, H., Neumaier, S., Guibert, P. & Zink, A. C. Environmental gamma dosimetry with OSL of  $\alpha\text{-Al}_2\text{O}_3\text{:C}$  for *in situ* sediment measurements. *Radiat. Prot. Dosimetry* **141**, 27–35 (2010).
- Richter, D. & Krbetschek, M. Luminescence dating of the Lower Palaeolithic occupation at Schöningen. *J. Hum. Evol.* **89**, 46–56 (2015).
- Schwarcz, H. P. Current challenges to ESR dating. *Quat. Sci. Rev.* **13**, 601–605 (1994).
- Mercier, N., Valladas, H. & Valladas, G. Observations on palaeodose determination with burnt flints. *Anc. TL* **10**, 28–32 (1992).
- Mercier, N. Flint palaeodose determination at the onset of saturation. *Int. J. Rad. Appl. Instrum. D* **18**, 77–79 (1991).
- Valladas, G. & Gillot, P. Y. Dating of the Olby lava flow using heated quartz pebbles: some problems. *PACT* **2**, 141–150 (1978).
- Richter, D. Advantages and limitations of thermoluminescence dating of heated flint from Paleolithic sites. *Geoarchaeology* **22**, 671–683 (2007).
- Joannes-Boyau, R. & Grün, R. A comprehensive model for CO<sub>2</sub> radicals in fossil tooth enamel: implications for ESR dating. *Quat. Geochronol.* **6**, 82–97 (2011).
- Grün, R. An alternative model for open system U-series/ESR age calculations: (closed system U-series)-ESR, CSUS-ESR. *Anc. TL* **18**, 1–4 (2000).
- Grün, R. et al. Direct dating of Florisbad hominid. *Nature* **382**, 500–501 (1996).
- Ramos, J. et al. The Benzu rockshelter: a Middle Palaeolithic site on the north African coast. *Quat. Sci. Rev.* **27**, 2210–2218 (2008).
- Adler, D. S. et al. Early Levallois technology and the Lower to Middle Paleolithic transition in the southern Caucasus. *Science* **345**, 1609–1613 (2014).
- Larrasoana, J. in *Modern Origins: A North African Perspective* (eds Hublin, J.-J. & McPherron, S. P.) 19–34 (Springer, 2012).
- Geraads, D. Biogeographic relationships of Pliocene and Pleistocene north-western African mammals. *Quat. Int.* **212**, 159–168 (2010).
- Prescott, J. R. & Hutton, J. T. Cosmic ray contributions to dose rates for luminescence and ESR dating: large depths and long-term time variations. *Radiat. Meas.* **23**, 497–500 (1994).

**Supplementary Information** is available in the online version of the paper.

**Acknowledgements** The Jebel Irhoud project is jointly conducted and supported by the Moroccan Institut National des Sciences de l'Archéologie et du Patrimoine and the Department of Human Evolution of the Max Planck Institute for Evolutionary Anthropology (MPI-EVA). We thank S. Albert (MPI-EVA) for sample preparation and for measuring the flint samples, E. Pernicka (Curt-Engelhorn-Zentrum Archäometrie, Mannheim) for neutron activation analysis and D. Degering (Verein für Kernverfahrenstechnik und Analytik, Rossendorf) for performing  $\gamma$ -ray spectrometry. The Max Planck Society funded the fieldwork and the thermoluminescence analysis. V. Aldeias (MPI-EVA) excavated the partial skull. B. Larmignat illustrated the stone artefacts. Philipp Gunz commented on the manuscript, and Les Kinsley (RSES, ANU) assisted with laser ablation measurements. Parts of the US/ESR research were funded by ARC discovery grants (DP0664144 to R.G.) and (DP140100919 to R.J.-B.)

**Author Contributions** Thermoluminescence dating was carried out by D.R.: ESR dating was done by R.G. and R.J.-B.; zooarchaeology and taphonomy was carried out by F.A., T.E.S. and D.G.; lithics analysis was done by S.P.M.; raw material analysis was carried out by P.F. and J.P.R.; geology was done by J.-P.R., P.F. and M.R.; and A.B.-N., J.-J.H. and S.P.M. excavated the site. D.R. and S.P.M. wrote the paper with contributions from all authors.

**Author Information** Reprints and permissions information is available at [www.nature.com/reprints](http://www.nature.com/reprints). The authors declare no competing financial interests. Readers are welcome to comment on the online version of the paper. Publisher's note: Springer Nature remains neutral with regard to jurisdictional claims in published maps and institutional affiliations. Correspondence and requests for materials should be addressed to S.P.M. ([mcpherron@eva.mpg.de](mailto:mcpherron@eva.mpg.de)).

**Reviewer Information** *Nature* thanks R. G. Klein, R. G. Roberts and the other anonymous reviewer(s) for their contribution to the peer review of this work.

## METHODS

**Thermoluminescence.** Thermoluminescence dating of heated flint artefacts is based on the accumulation of metastable charges (palaeodose) in the crystal lattice by ionizing radiation since the last heating of the rock<sup>32</sup>. The method provides an age estimate of a prehistoric activity and therefore of human behaviour directly<sup>23</sup>. An age is obtained by the ratio of the palaeodose, determined with thermoluminescence, to the total effective dose-rate, with the assumption that the dose-rate was constant over the entire burial time<sup>32</sup>.

**Palaeodose determination.** Because the natural luminescence signal of the Jebel Irhoud samples is in the nonlinear part of the dose–response curve, the palaeodose on the 90–160  $\mu\text{m}$  fraction of the crushed and chemically treated flint material<sup>18,23</sup> (after the removal of the outer 2 mm surface with a cooled low-speed saw) was obtained by a multi-aliquot additive regeneration slide protocol<sup>18,20–22</sup> (Extended Data Fig. 7). Heated flint thermoluminescence dating results were obtained with this protocol for many other ancient sites<sup>33–35</sup>, where there was good agreement with other chronometric dates<sup>33,36–38</sup>. The thermoluminescence data are described by exponential functions and shifted along the dose axis<sup>20–22</sup> to obtain the palaeodoses, similar to slide approaches for other materials<sup>39–41</sup>. Between 4 and 12 aliquots were used for each of the 3–5 dose points for each dose–response curve, where the grains used to construct the regeneration dose–response curve were heated to 360 °C for 90 min in air. This procedure is assumed to induce the least changes in sensitivity. However, only samples exhibiting unity of the thermoluminescence–signal ratios of the two dose–response curves after sliding (Extended Data Fig. 7) were accepted<sup>20</sup>. Comparable results, with many more samples passing the quality criteria, are obtained when the regeneration dose–response curves are scaled<sup>40,41</sup>, an approach that has provided congruent results in comparison to other luminescence dating<sup>38</sup> analyses and/or when thermoluminescence glow peaks are aligned<sup>42</sup>. This larger sample set includes artefacts from the eastern part of the section, close to the hominins.

Thermoluminescence was measured with an EMI 9236QA photomultiplier with detection restricted to the UV-blue-wavelength band by Schott BG25 and WG5 filters at a heating rate of 5 K  $\text{min}^{-1}$  to 450 °C on a Risø DA-20 system. Irradiations were performed with external calibrated sources ( $\beta$  with  $^{90}\text{Y}/^{90}\text{Sr}$  at  $0.26 \pm 0.01$  Gy  $\text{s}^{-1}$  and  $\alpha$  with  $^{214}\text{Am}$  at  $0.178 \pm 0.011$   $\mu\text{m}^{-2}$   $\text{min}^{-1}$ ) and samples were stored before measurements (1 week at 70 °C or 4 weeks at room temperature). The  $\alpha$  sensitivity<sup>43</sup> was determined by comparing the regenerated luminescence response of 4–11- $\mu\text{m}$  fine-grained material (heated in air to 500 °C for 30 min) to single doses of  $\alpha$  and  $\beta$  irradiation. The doses were chosen to produce thermoluminescence signals at similar levels, while staying well within a linear dose–response. Whether the thermoluminescence signal was sufficiently zeroed was analysed for the 45 flint artefacts that showed macroscopic traces of heating with the heating plateau test<sup>32</sup> (inset in Extended Data Fig. 7). Of these, 14 artefacts eventually passed the described tests (Table 1 and Extended Data Table 2). The integration range of the luminescence signal for palaeodose determination was defined by the heating plateau (Extended Data Table 2).

**Dosimetry.** The calculations of internal dose-rates<sup>44</sup> are based on neutron activation analysis results (Extended Data Table 2) for U, Th and K of 200 mg sample material of less than 160  $\mu\text{m}$  from the material after sawing that was obtained before the chemical treatment and further sieving.

Dosimetric dating methods are based on the assumption of stability of the dose-rates over the burial time and that radioactive elements are homogeneously distributed throughout the sample. However, either can be modelled as well<sup>45,46</sup>. Heterogeneous internal dose-rates from inhomogeneities in radioactive element distributions have been shown to be limited to macroscopically visible veins, inclusions and different mineral phases<sup>47</sup>. These are not observed here and any altered parts were removed<sup>23</sup>. At Jebel Irhoud, the internal dose-rate provides variable accounts of the total dose-rate ranging between 20% and 55% (Table 1).

The stability over time of the external  $\gamma$ -dose-rate from the surrounding sediment was verified by HpGe  $\gamma$ -ray spectrometry (based on an estimated matrix of 95%  $\text{SiO}_2$  and 5%  $\text{BaSO}_4$  to accommodate for the ubiquitous presence of barite) on sediment samples (grain fraction less than around 40 mm in particle diameter). There is no indication of disequilibria for either the U or the Th decay chain (Extended Data Table 2b) in the entire sediment column. While these analyses do not reject the possibility of very ancient occurrences of disequilibria, we interpret the lack of such and the absence of any trends in ratios of analysed isotopes through the sediment column as indications that the decay chains have always been in equilibrium. The absence of significant changes in the external  $\gamma$ -dose-rate is also indicated by the age results of samples with the highest internal dose-rates (Table 1 and Extended Data Table 2), which can be considered to be more reliable<sup>23</sup>. They provide results in the upper as well as in the lower range of the age dispersion, which would not be expected for samples of the same age suffering from fluctuating  $\gamma$ -dose-rates. We assume, therefore, that the external  $\gamma$ -dose-rate was stable over the entire burial period.

HpGe  $\gamma$ -ray spectrometry allows analysis of only the small sediment particles, but Jebel Irhoud contains larger rocks and especially large boulders in the lower sequence. HpGe  $\gamma$ -ray spectrometry on sediment samples in the laboratory is, therefore, not representative of the spatial heterogeneity and the site's dosimetry has to be considered as 'lumpy'<sup>19</sup>.

The external  $\gamma$ -doses were measured with  $\alpha$ - $\text{Al}_2\text{O}_3\text{:C}$  dosimeters. These were left buried 30 cm into all of the exposed profiles for one year with 60 cm spacing between dosimeters to measure all available layers (Extended Data Table 2a). The dosimeters record the cosmic and  $\gamma$ -dose-rates at their individual positions, the latter of which are assumed to be similar to those of the excavated flint samples coming from different positions within a given layer. The  $\gamma$ -dose-rates are obtained by comparing each crystal's OSL response (an average of five for each dosimeter) of the natural one-year exposure to an irradiation by a calibrated  $^{137}\text{Cs}$ -source. The high accuracy and precision of this approach has recently been shown by comparison with HpGe  $\gamma$ -ray spectrometry<sup>17</sup>. The present day cosmic dose differs from that of the past due to the recent removal of overlying rock and sediment, and therefore the measured values have to be adjusted. The nearly vertical, 4 m high, rock wall at a maximum distance of only around 1.5 m from the dosimeters provides approximately 50% shielding on one side in addition to the sediment that covers them. Thus cosmic doses were calculated separately for the full  $4\pi$  geometries of 4 m rock overburden, as well as for the present day sediment coverage, and then adjusted by 50% each and summed.

Analytical uncertainties for dosimeter measurements are typically between 2% and 5%, but for age calculation a conservative uncertainty of 15% was used for the averaged external  $\gamma$ -dose-rates, which is larger than the dispersion of the dosimeter readings. The sublayers of layer 7 (Figs 1, 2) are defined in part by the slight syn- or post-depositional process of localized weak brecciation, which probably has led to differences in the external  $\gamma$ -dose-rate related to this geochemical process of fixation of the sediment of layer 7C. The  $\gamma$ -dosimetry from each sublayer (as defined by consolidated appearance and not necessarily in superposition) was used for age calculation. On the basis of archaeological and sedimentological interpretation, which indicate a common age for all material from layer 7, but not necessarily the same dosimetry, the average ages are reported as a single context age for layer 7.

Excavation and mining activities removed the roof and most of the sediments, exposing the present day sediments for several decades. Prior to the 1960s, the site was an almost completely filled and sealed cave, and it is likely that sediments were moister in this context. Therefore, present day  $\gamma$ -dose-rates are likely to be overestimated and thus the resulting ages slightly too young. Because there is little data to estimate the moisture for the entire burial history, we conservatively use the present day moisture (Extended Data Table 2), which is included in the dosimeter readings, and thus we consider our thermoluminescence ages to be minimum estimates. The influence of moisture content on the calculated ages is, however, not large. For example, an increase in moisture by 20% would result, on average, in an increase in the ages by only about 10%. As expected, the  $\gamma$ -dose-rates deduced from *in situ* dosimeters are between 8% and 30% lower compared to HpGe  $\gamma$ -ray spectrometry data that was corrected for the moisture as measured from sealed sediment samples (Extended Data Table 2c).

To estimate the past cosmic dose-rate we used a section drawing<sup>48</sup>, which provides a scale and section drawings<sup>49,50</sup>, where the positions of the human skulls from the previous excavations are marked, as well as historical photos showing that the recent excavation is located to the south of the previous excavations. Our link to the Tixier excavation<sup>12</sup> was supported in part by a nail still present in one of the profiles. In order to calculate the cosmic dose-rates (Extended Data Table 2) the overburden of sediment and rock (assumed densities of 1.9 and 2.4 g  $\text{cm}^{-3}$ , respectively) were estimated by connecting the surface of the rock coverage to the north and to the south (rock that has since been removed by human activities). This results in a minimum rock thickness of 6 m for the roof and 3–4 m of sediment in the cave, where approximately 3 m of sediment covered the recent hominin finds.

**Estimation of the age of layers 6 and 7.** Analysis of the thermoluminescence ages of layers 4 and 5 is hampered by the low number of samples. For layers 6 and 7 the relative standard deviations of the ages (9% and 6%, respectively) are similar to the relative standard deviations of dosimeter readings (8% and 12%, respectively), and the same applies to the relative average deviations from the means (for layers 6 and 7 these are 9% and 5% for ages; 6% and 11% for dosimeter results, respectively) as a measure of the variability of the data.

For dosimetric dating of objects (thermoluminescence of heated flint artefacts or ESR on teeth) from heterogeneous sediments the external  $\gamma$ -dose-rate for each individual sample cannot be known per se, because the sample is removed from its context during excavation and the measurement of the  $4\pi$  external  $\gamma$ -dose-rate is not possible at each sample's original location.  $\gamma$ -dose-rates, therefore, have to be either reconstructed<sup>51–53</sup> or averaged results must be used<sup>18,19,23,34,35,54</sup>. For heterogeneous sediments the average value of dosimeter measurements is unlikely to be correct for any of the samples<sup>18</sup>. However, for the above reasons, the nearest

neighbouring dosimeter will not necessarily provide a better estimate of the external  $\gamma$ -dose-rate either, because it might not have been exposed in the exact same geometry. Nevertheless, provided that the samples were heated at roughly the same time, an age estimate close to the true mean can be obtained based on averaged external  $\gamma$ -dosimetry. It is assumed that dosimeter positions are similar to the ones occupied by the samples in the sediment and, therefore, either geometry can be considered as random, because no selection is possible for either. This means that individual dose-rates and ages should be randomly dispersed about the mean  $\gamma$ -dose-rate<sup>18,19,23</sup>. As a consequence, this lack of knowledge of the true external  $\gamma$ -dose-rate leads to a large spread in individual apparent thermoluminescence age data (Table 1), but the mean age from several samples then provides a meaningful age estimate of the last heating<sup>18,19,23</sup>.

Basic statistical analysis is only possible for layers 6 and 7. Shapiro–Wilk tests (software package Origin 8.5) showed that the two datasets ( $W$  values of 0.92 and 0.91 for layers 6 and 7, respectively) are samples from normal distributions at the 0.05 probability level ( $W$  threshold values of 0.52 and 0.41, respectively). We treat each of the major geologically defined stratigraphic layers as analytical units, therefore providing the minimum resolution, and we calculate weighted average ages for each. The last heating of the sampled flint artefacts is estimated to have occurred  $302 \pm 32$  ka for layer 6 and  $315 \pm 34$  ka for layer 7 at the  $1\sigma$  probability level. These weighted average ages were calculated with the individual statistical uncertainties, deriving mainly from the luminescence measurements, as weights. The uncertainties considered as mainly systematic, for example, source calibration, were subsequently added and the uncertainty estimate of the weighted average is derived from both uncertainties summed in quadrature. The two population means for layers 6 and 7 are not different at a level of 0.05 with a two sample  $t$ -test ( $P$  values of 0.09 and 0.12 for equal and unequal assumed variance, respectively, from software package Origin 8.5). The thermoluminescence determinations provide nominal age ranges at 95% probability of 366–238 kyr for layer 6 and 383–247 kyr for layer 7, which contains the hominin remains. Analysing the same data with an extrapolation approach<sup>32</sup> for both dose–response curves provides very similar palaeodoses, resulting in weighted mean ages which are different by only a few per cent.

It can be concluded that the sequence of sediments containing the archaeological and palaeoanthropological material is about 300 kyr old.

**ESR.** A fragment of a single tooth from the Irhoud 3 mandible was dated by coupled US/ESR to  $160 \pm 16$  ka (ref. 10). This method has been shown to provide comparable results when critically appraised against other dating results and verified independent chronologies<sup>37,55–57</sup>. The dosimetry was based on radionuclide analysis of a sediment sample argued to be from the same brecciated layers from which the fossils were thought to derive. Here the age is recalculated due to recent insights into the dose estimation of enamel fragments<sup>24</sup> and the availability of more detailed dosimetric data.

**Dose determination.** The ESR dating signal consists of several types of  $\text{CO}_2^-$  radicals, two anisotropic, orientated (axial and orthorhombic) and one non-oriented radical. When the enamel fragment is rotated between ESR measurements, the intensities of the orientated  $\text{CO}_2^-$  radicals change, whereas the intensity of the non-oriented radical remains constant<sup>24</sup>. The natural ESR signal of Irhoud contains about 90% and 10% of anisotropic and non-oriented  $\text{CO}_2^-$  radicals, respectively (Extended Data Fig. 8). By contrast, the laboratory-generated ESR intensity contains  $40 \pm 2\%$  non-oriented  $\text{CO}_2^-$  radicals. Unfortunately, some of these are thermally unstable. Different enamel domains with significantly different dose-responses (figure 6 in ref. 24), show that some of the laboratory induced, non-oriented  $\text{CO}_2^-$  radicals are stable (around 10%) and around 35% are likely to convert into stable anisotropic  $\text{CO}_2^-$  radicals over time.

The ESR signals of the enamel piece from Irhoud 3 were decomposed following ref. 24. Extended Data Fig. 8 shows the assessment of the percentage of non-oriented  $\text{CO}_2^-$  radicals in the overall signal intensity of the natural and irradiated samples. The decomposition results have relatively large individual errors (around 5% for each value) but the data can be fitted with a single saturating function, which then provides the amount of non-oriented  $\text{CO}_2^-$  radicals for each radiation step. Fitting only the anisotropic  $\text{CO}_2^-$  radicals yields a dose value of  $383 \pm 8$  Gy. However, because of the probable transfer of non-oriented to stable anisotropic  $\text{CO}_2^-$  radicals, the dose is somewhat smaller. The samples from Holon<sup>24</sup> and Irhoud have similar ages and also similar amounts of non-oriented  $\text{CO}_2^-$  radicals in the laboratory-generated ESR signal. Assuming that  $45 \pm 5\%$  of the laboratory-generated non-oriented  $\text{CO}_2^-$  radicals are either stable or are converted into anisotropic  $\text{CO}_2^-$  radicals, a dose of  $326 \pm 16$  Gy is obtained (Extended Data Table 3), which is about 26% higher than previously reported<sup>10</sup>. The fragment was scanned with quadrupole laser ablation ICP-MS in order to obtain the spatial uranium distribution in enamel and dentine<sup>38</sup>. Uranium concentrations average at  $0.07 \pm 0.04$  p.p.m. and  $3.76 \pm 0.42$  p.p.m. in enamel and dentine, respectively. The U-concentrations in the enamel are too low for *in situ* U-series analysis. Using the multi-collector laser

ablation ICP-MS system<sup>59,60</sup>, the dentine was analysed for U-series isotopes and yielded ratios of  $1.5287 \pm 0.0088$  for  $^{234}\text{U}/^{238}\text{U}$  and  $0.7186 \pm 0.0114$  for  $^{230}\text{Th}/^{234}\text{U}$ . **Dosimetry.** We assume here that the mandible originates from sediments equivalent to layer 7 based on published accounts<sup>50,61</sup> indicating that the hominin remains, including the mandible, originated from the lower part of the section. Although the original position and thus precise sedimentological association is unknown, assuming an origin from any of the other sediment layers would not provide significantly different age results because of the similar dosimetry of all layers (Extended Data Table 2). Dosimetry based on dosimeters is preferred because the heterogeneity (lumpiness) of the sediment is accounted for, which was previously not the case<sup>10</sup>. The average  $\gamma$ -dose-rate measured *in situ* by the dosimeters (Extended Data Table 2a) for layer 7 provides  $807 \pm 107 \mu\text{Gy a}^{-1}$ . To account for the interaction of shielding and dosing of the mandible<sup>62</sup>, the external  $\gamma$ -dose-rate was adjusted by 7%, resulting in an effective external  $\gamma$ -dose-rate of  $751 \pm 100 \mu\text{Gy a}^{-1}$ . An additional cosmic dose-rate component of  $70 \pm 7 \mu\text{Gy a}^{-1}$  has to be considered. Total radionuclide concentrations from Hp-Ge  $\gamma$ -spectrometry of the sediment yielded  $2.37 \pm 0.67$  p.p.m. U;  $6.77 \pm 0.47$  p.p.m. Th and  $2.32 \pm 0.22\%$  K (calculated from the average of layer 7 from Extended Data Table 2b). These data are different from those previously used<sup>10</sup>, where the relative distribution of Th and U was  $1.6 \pm 0.1$  p.p.m. and  $6.98 \pm 0.1$  p.p.m., respectively. This seems to point to a mix up of the Th and U values in the previous study<sup>10</sup>. The measured values for layer 7 were used for the water content of the sediments (Extended Data Table 2c), and 5% water in the dentine is assumed. The enamel thickness varied along the fragment and was on average  $1,000 \pm 200 \mu\text{m}$ .

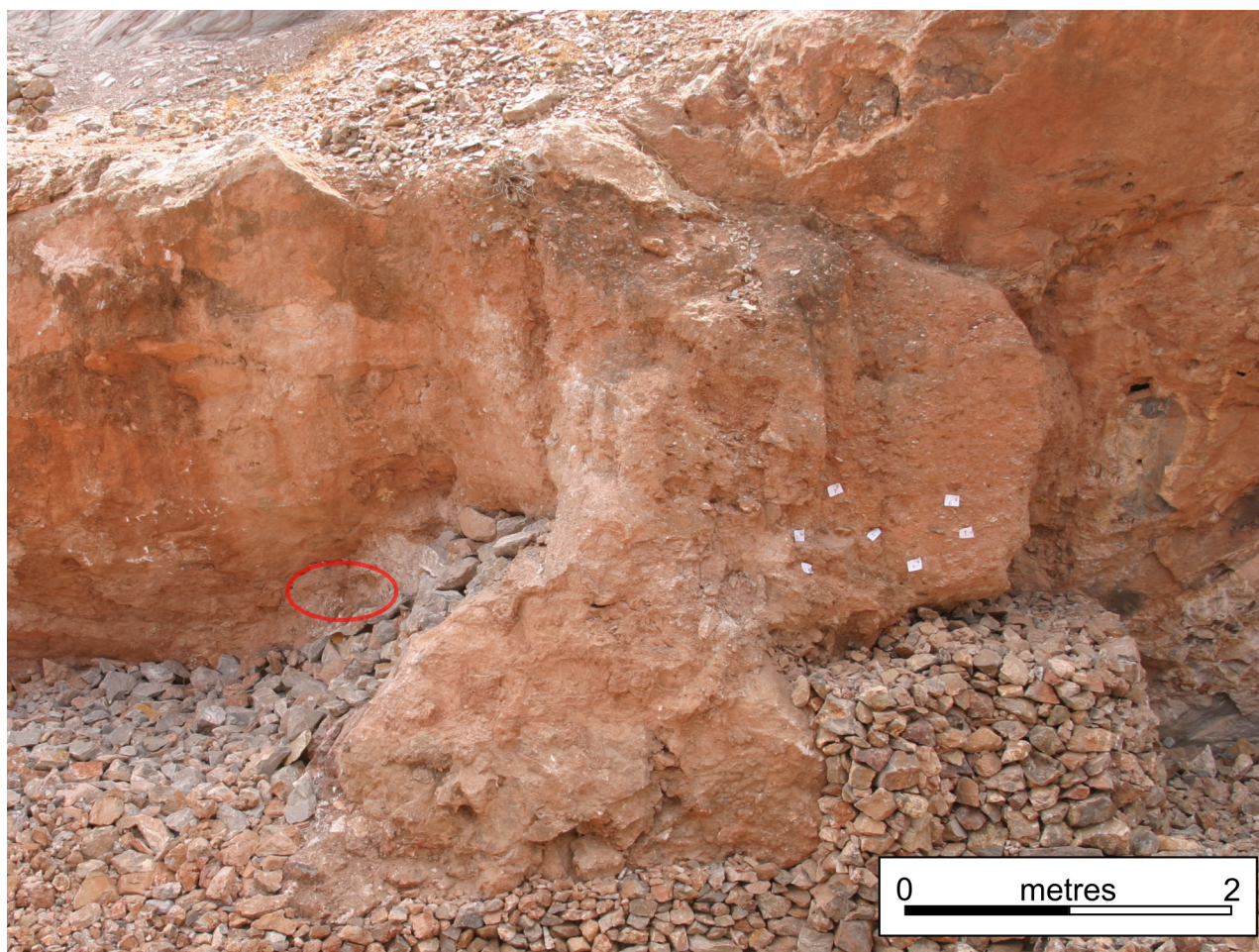
Since no external layer was removed from the enamel fragment, the external  $\alpha$ -dose-rate has to be considered. The average nuclide concentrations from HpGe  $\gamma$ -ray spectrometry (Extended Data Table 2b) of layer 7 combined with an assumed  $0.13 \pm 0.02 \alpha$  efficiency<sup>63</sup> and attenuation factors<sup>64</sup> provide an average external  $\alpha$ -dose-rate of  $6 \pm 1 \mu\text{Gy a}^{-1}$  from U and Th (Extended Data Table 3). The dentine generates a dose in the enamel of less than 0.5 Gy, which was not considered further.

**Sample size.** No statistical methods were used to predetermine sample size.

**Data availability.** The authors declare that the data supporting the findings of this study are available within the article and its Supplementary Information.

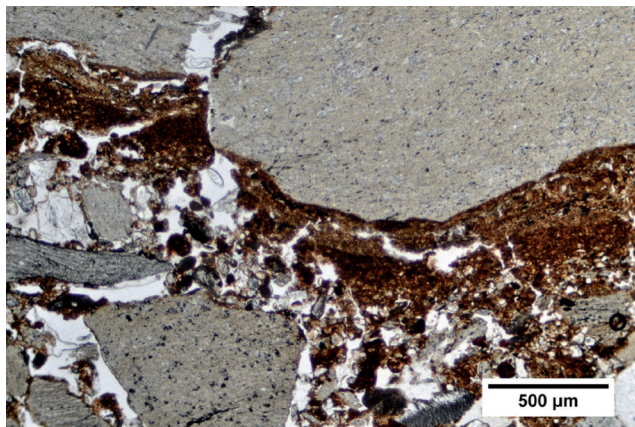
32. Aitken, M. J. *Thermoluminescence Dating* (Academic, 1985).
33. Mercier, N. & Valladas, H. Reassessment of TL age estimates of burnt flints from the Paleolithic site of Tabun Cave, Israel. *J. Hum. Evol.* **45**, 401–409 (2003).
34. Valladas, H. *et al.* Thermoluminescence dates for the Neanderthal burial site at Kebara in Israel. *Nature* **330**, 159–160 (1987).
35. Valladas, H. *et al.* Thermoluminescence dating of mousterian 'Trotto-Cro-Magnon' remains from Israel and the origin of modern man. *Nature* **331**, 614–616 (1988).
36. Rink, W. J., Schwarcz, H. P., Ronen, A. & Tsatskin, A. Confirmation of a near 400 ka age for the Yabrudian industry at Tabun Cave, Israel. *J. Archaeol. Sci.* **31**, 15–20 (2004).
37. Mercier, N. *et al.* New datings of Amudian layers at Qesem Cave (Israel): results of TL applied to burnt flints and ESR/U-series to teeth. *J. Archaeol. Sci.* **40**, 3011–3020 (2013).
38. Frouin, M. *et al.* Chronology of the Middle Palaeolithic open-air site of Combe Brune 2 (Dordogne, France): a multi luminescence dating approach. *J. Archaeol. Sci.* **52**, 524–534 (2014).
39. Prescott, J. R., Huntley, D. J. & Hutton, J. T. Estimation of equivalent dose in thermoluminescence dating — the Australian slide method. *Anc. TL* **11**, 1–5 (1993).
40. Sanzelle, S., Miallier, D., Pilleyre, T., Faïn, J. & Montret, M. A new slide technique for regressing TL/ESR dose response curves—intercomparison with other techniques. *Radiat. Meas.* **26**, 631–638 (1996).
41. Guibert, P., Vartanian, E., Bechtel, F. & Schvoerer, M. Non linear approach of TL response to dose: polynomial approximation. *Anc. TL* **14**, 7–14 (1996).
42. Berger, G. W. Thermoluminescence dating studies of rapidly deposited silts from south-central British Columbia. *Can. J. Earth Sci.* **22**, 704–710 (1985).
43. Valladas, H. & Valladas, G. Effect de l'irradiation alpha sur des grains de quartz. *PACT* **6**, 171–179 (1982).
44. Adamiec, G. & Aitken, M. Dose-rate conversion factors: update. *Anc. TL* **16**, 37–50 (1998).
45. Guibert, P., Lahaye, C. & Bechtel, F. The importance of U-series disequilibrium of sediments in luminescence dating: a case study at the Roc de Marsal Cave (Dordogne, France). *Radiat. Meas.* **44**, 223–231 (2009).
46. Tribolo, C. *et al.* TL dating of burnt lithics from Blombos Cave (South Africa): further evidence for the antiquity of modern human behaviour. *Archaeometry* **48**, 341–357 (2006).
47. Schmidt, C., Rufer, D., Preusser, F., Krbetschek, M. & Hilgers, A. The assessment of radionuclide distribution in silex by autoradiography in the context of dose rate determination for thermoluminescence dating. *Archaeometry* **55**, 407–422 (2013).
48. Ennouchi, E. Essai de datation du gisement de Jebel Irhoud (Maroc). *Comptes Rendus Somm. Séances Société. Geol. Fr.* **10**, 405–406 (1966).

49. Arambourg, C. Le gisement moustérien et l'homme du Jebel Irhoud. *Quaternaria* **7**, 1–7 (1965).
50. Ennouchi, E. Le site du Jebel Irhoud (Maroc). in *Actas del V Congreso Panafricano de Prehistoria y de Estudio del Cuaternario (Santa Cruz de Tenerife, 1963)* **6**, 53–60 (1966).
51. Guibert, P., Bechtel, F., Schvoerer, M., Müller, P. & Balescu, S. A new method for gamma dose-rate estimation of heterogenous media in TL dating. *Radiat. Meas.* **29**, 561–572 (1998).
52. Guérin, G. *Modélisation et Simulations Numérique des Effets Dosimétriques dans les Sediments Quaternaires: Application aux Méthodes de Datation par Luminescence*. PhD thesis, Univ. Bordeaux (2012).
53. Guérin, G. & Mercier, N. Field gamma spectrometry, Monte Carlo simulations and potential of non-invasive measurements. *Geochronometria* **39**, 40–47 (2012).
54. Mercier, N., Valladas, H., Valladas, G. & Reyss, J.-L. TL dates of burnt flints from Jelinek's excavations at Tabun and their implications. *J. Archaeol. Sci.* **22**, 495–509 (1995).
55. Falguères, C. *et al.* Combined ESR/U-series chronology of Acheulian hominid-bearing layers at Trinchera Galería site, Atapuerca, Spain. *J. Hum. Evol.* **65**, 168–184 (2013).
56. Michel, V., Delanghe-Sabatier, D., Bard, E. & Ruiz, C. B. U-series, ESR and  $^{14}\text{C}$  studies of the fossil remains from the Mousterian levels of Zafarraya Cave (Spain): a revised chronology of Neandertal presence. *Quat. Geochronol.* **15**, 20–33 (2013).
57. Wagner, G. A. *et al.* Radiometric dating of the type-site for *Homo heidelbergensis* at Mauer, Germany. *Proc. Natl Acad. Sci. USA* **107**, 19726–19730 (2010).
58. Eggins, S., Grün, R., Pike, A. W. G., Shelley, M. & Taylor, L.  $^{238}\text{U}$ ,  $^{232}\text{Th}$  profiling and U-series isotope analysis of fossil teeth by laser ablation-ICPMS. *Quat. Sci. Rev.* **22**, 1373–1382 (2003).
59. Grün, R., Aubert, M., Joannes-Boyau, R. & Moncel, M.-H. High resolution analysis of uranium and thorium concentration as well as U-series isotope distributions in a Neanderthal tooth from Payre (Ardèche, France) using laser ablation ICP-MS. *Geochim. Cosmochim. Acta* **72**, 5278–5290 (2008).
60. Grün, R., Eggins, S., Kinsley, L., Moseley, H. & Sambridge, M. Laser ablation U-series analysis of fossil bones and teeth. *Palaeogeogr. Palaeoclimatol. Palaeoecol.* **416**, 150–167 (2014).
61. Ennouchi, E. Le deuxième crâne de l'homme d'Irhoud. *Ann. Paleontol. LIV*, 117–128 (1968).
62. Nathan, R. & Grün, R. Gamma dosing and shielding of a human tooth by a mandible and skull cap: Monte Carlo simulations and implications for the accuracy of ESR dating of tooth enamel. *Anc. TL* **21**, 79–84 (2003).
63. Grün, R. & Katzenberger-Apel, O. An alpha irradiator for ESR dating. *Anc. TL* **12**, 35–38 (1994).
64. Grün, R. Alpha dose attenuation in thin layers. *Anc. TL* **5**, 6–8 (1987).
65. Valladas, H. *Datation par la Thermoluminescence de Gisements Moustériens du Sud de la France* PhD Thesis, Univ. Paris VI (1985).

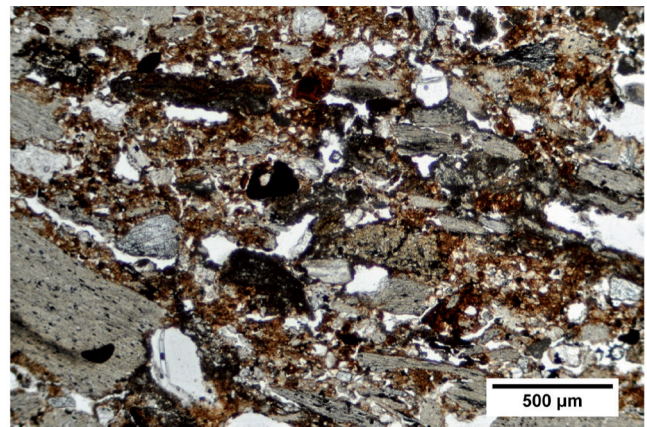


**Extended Data Figure 1 | View south of the remaining sediments at the start of excavations in 2004.** The approximate area of the main fossil concentration (not actually visible in this initial photograph taken before our excavations) is circled in red and detailed in Fig. 1b, c. The stacked

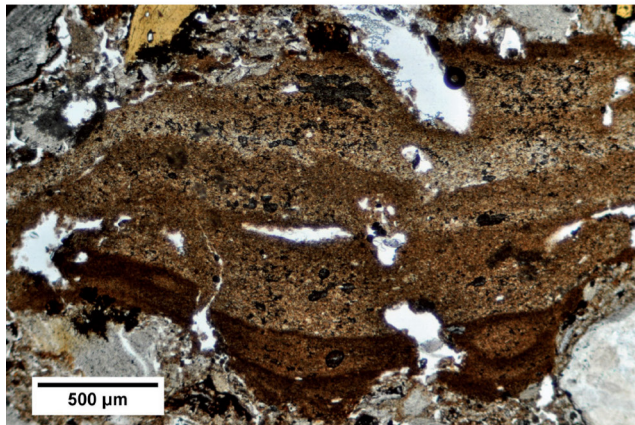
rocks around the base of the sediments and ramping up to the sediments on the left were placed there for protection of the remaining deposits. The white tags mark dosimeter locations. The scale is correct for the section with the tags.



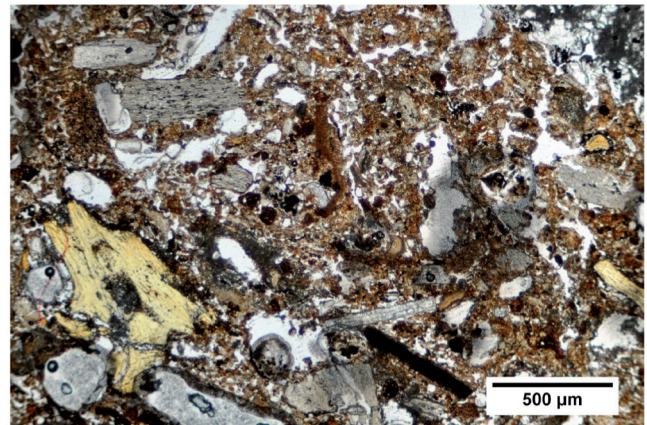
a



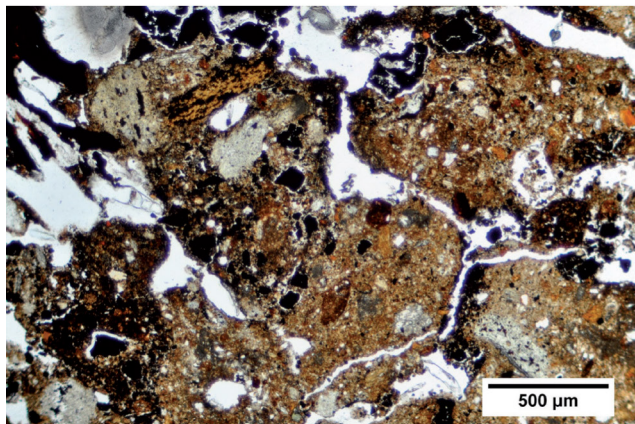
b



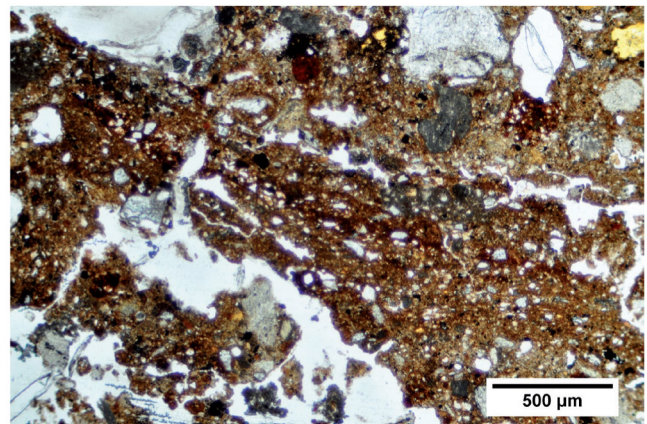
c



d



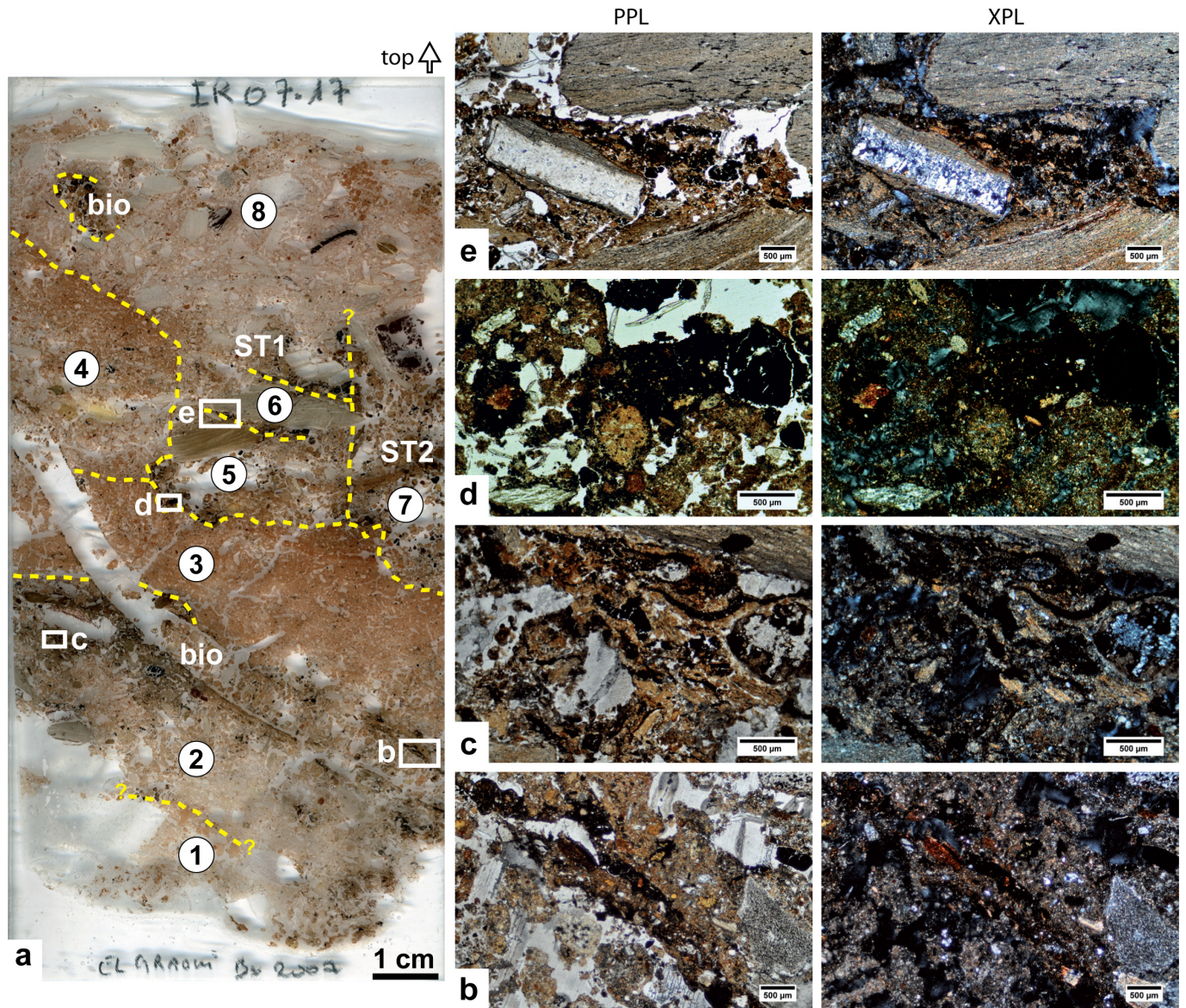
e



f

**Extended Data Figure 2 | Non-polarized light photomicrographs from thin-sections.** a, Layer 4, thin-section 608M, showing the good preservation of the sediment owing to overlying cave lithoclasts. b, Layer 4, thin-section 608M, clasts are oriented with unit dip. c, Layer 7 upper part, thin-section 712T, indicating a run-off deposit. d, Layer 7, thin-section

609T, bone micro-fragments in an isotropic fabric microfacies. e, Lower part of layer 7, thin-section 716, with a high density of micro-charcoal, soil aggregates, bone fragments and heated lithoclasts. f, Trampled surface in layer 7, thin-section 712B (thin sections by M. El Graoui). Photos by M.R.

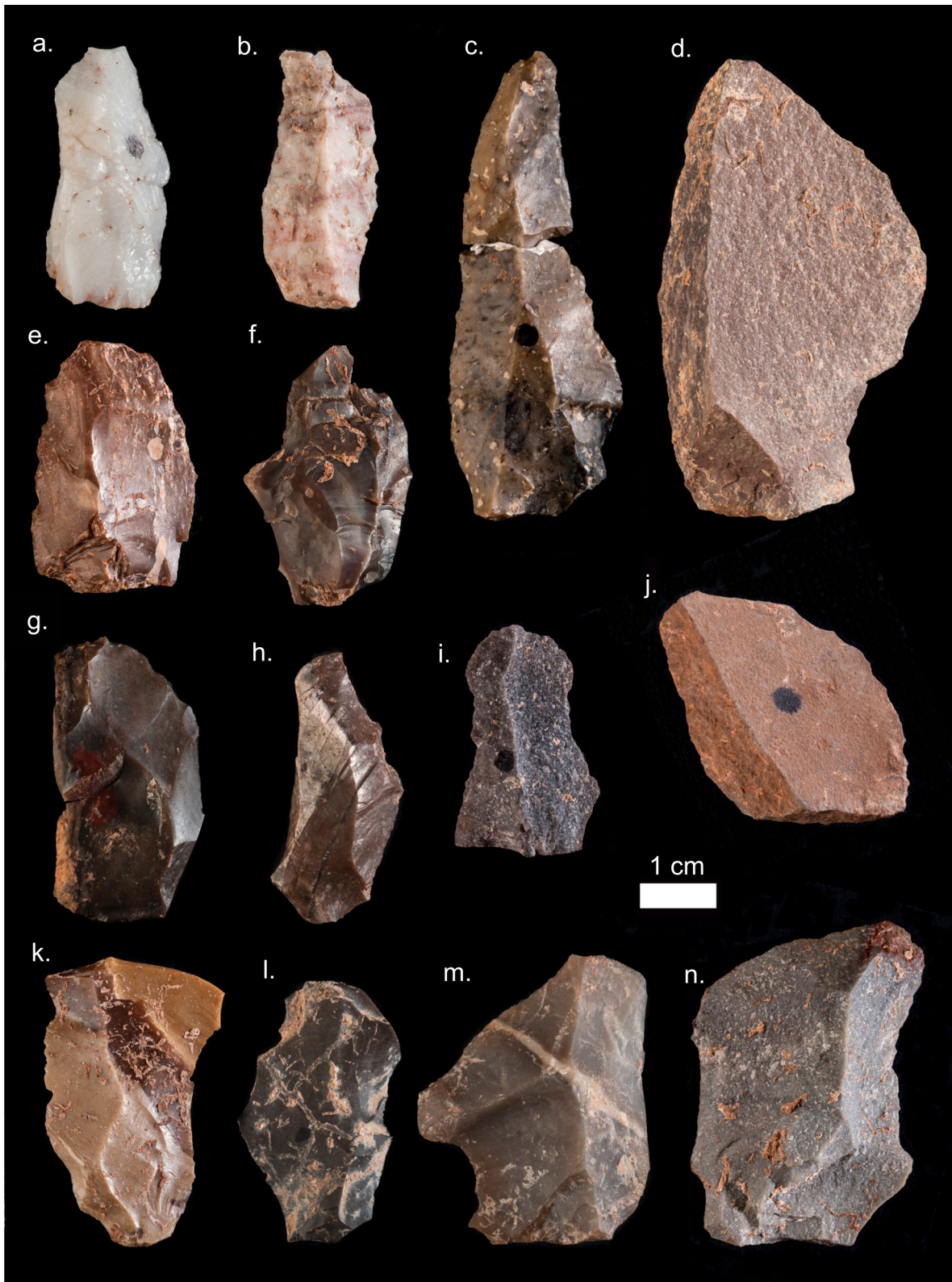


**Extended Data Figure 3 | Cross-polarized and plane-polarized photomicrographs from thin-section of micromorphology sample 717 (layer 7).** a, Scanned thin section. Squares with letters in a refer to the areas in b–e, each area provided as plane- (PPL) and cross-polarized (XPL) images. Scale bar, 0.5 mm. Bio indicates bioturbation and the numbers

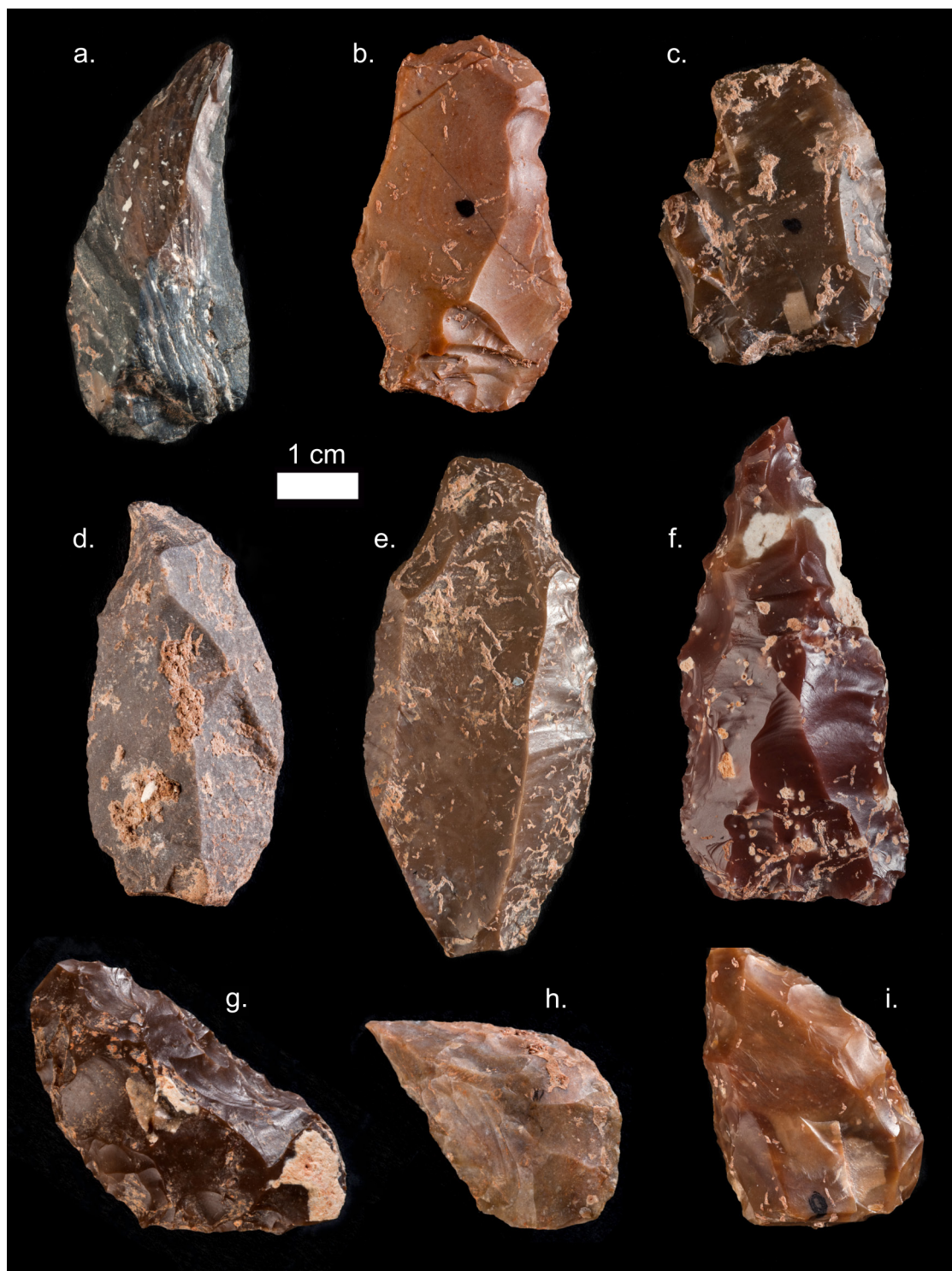
refer to the sub-units as indicated by dotted lines. ST refers to structure. b, Black coatings against a biogallery wall. c, Micro-bedded carbon products preserved under a schisteous clast. d, Carbon aggregates that coat the bottom of ST1. e, bed of carbon micro-particles in the filling of ST1. Photos by M.R.



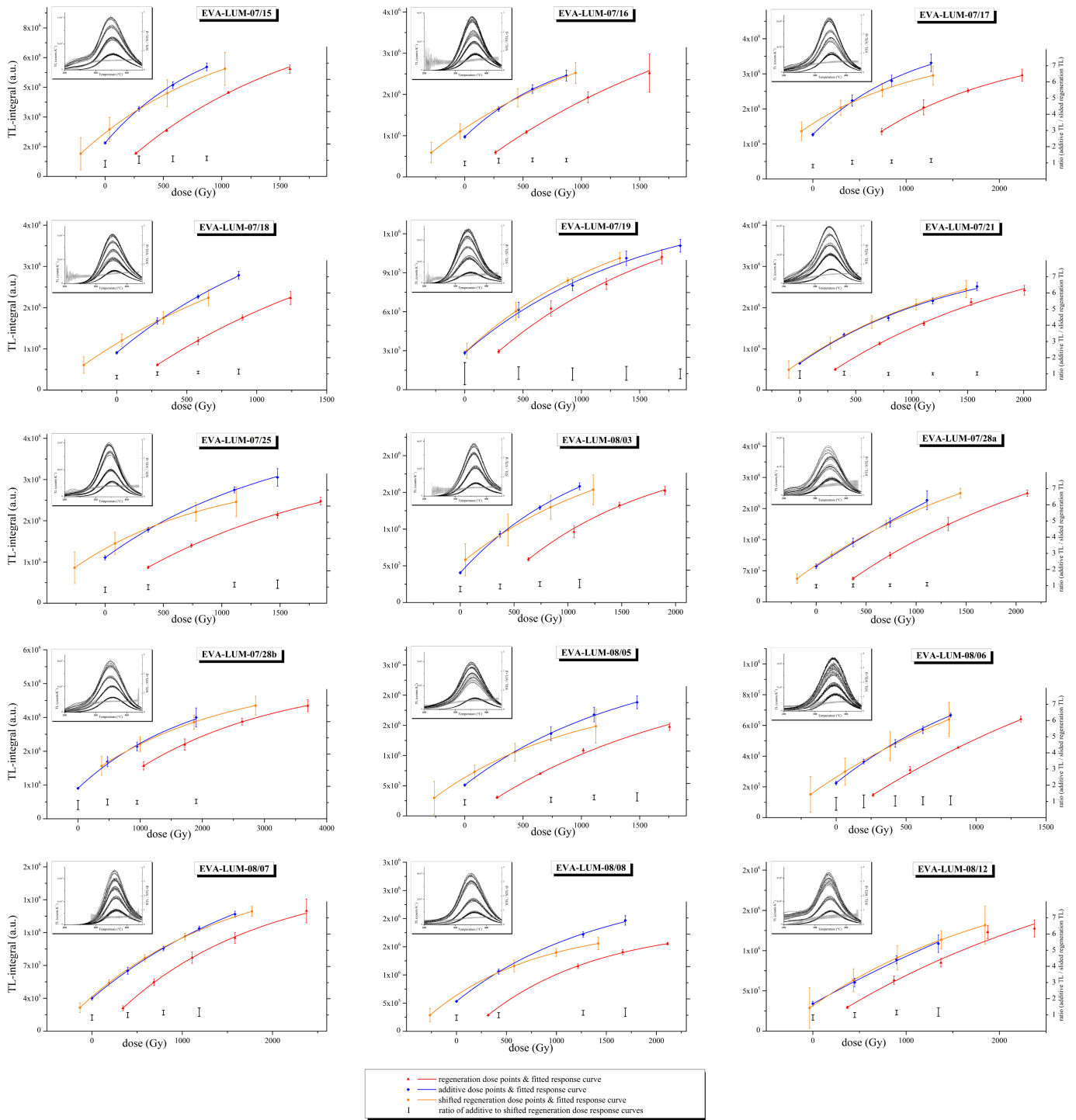
**Extended Data Figure 4 | Flint artefacts.** a, b, e, Unifacial points (layer 6). c, d, Convergent scrapers (layer 6). f, Déjeté scraper (layer 6). g, h, Convergent scrapers (layer 7). i, Unifacial point (layer 7). j, Levallois Flake (layer 7). k, m, Double scrapers (layer 7). l, Déjeté scraper (layer 7). n, Single scraper (layer 7).



**Extended Data Figure 5 | Stone artefacts from layer 7.** a, b, Quartz flakes. c, m, Flint Levallois flakes. d, i, Silicified limestone flakes. e, g, h, Flint flakes with some edge damage. f, Flint flake. j, n, Silicified limestone flakes with some edge damage. k, l, Flint Levallois flakes with some edge damage.

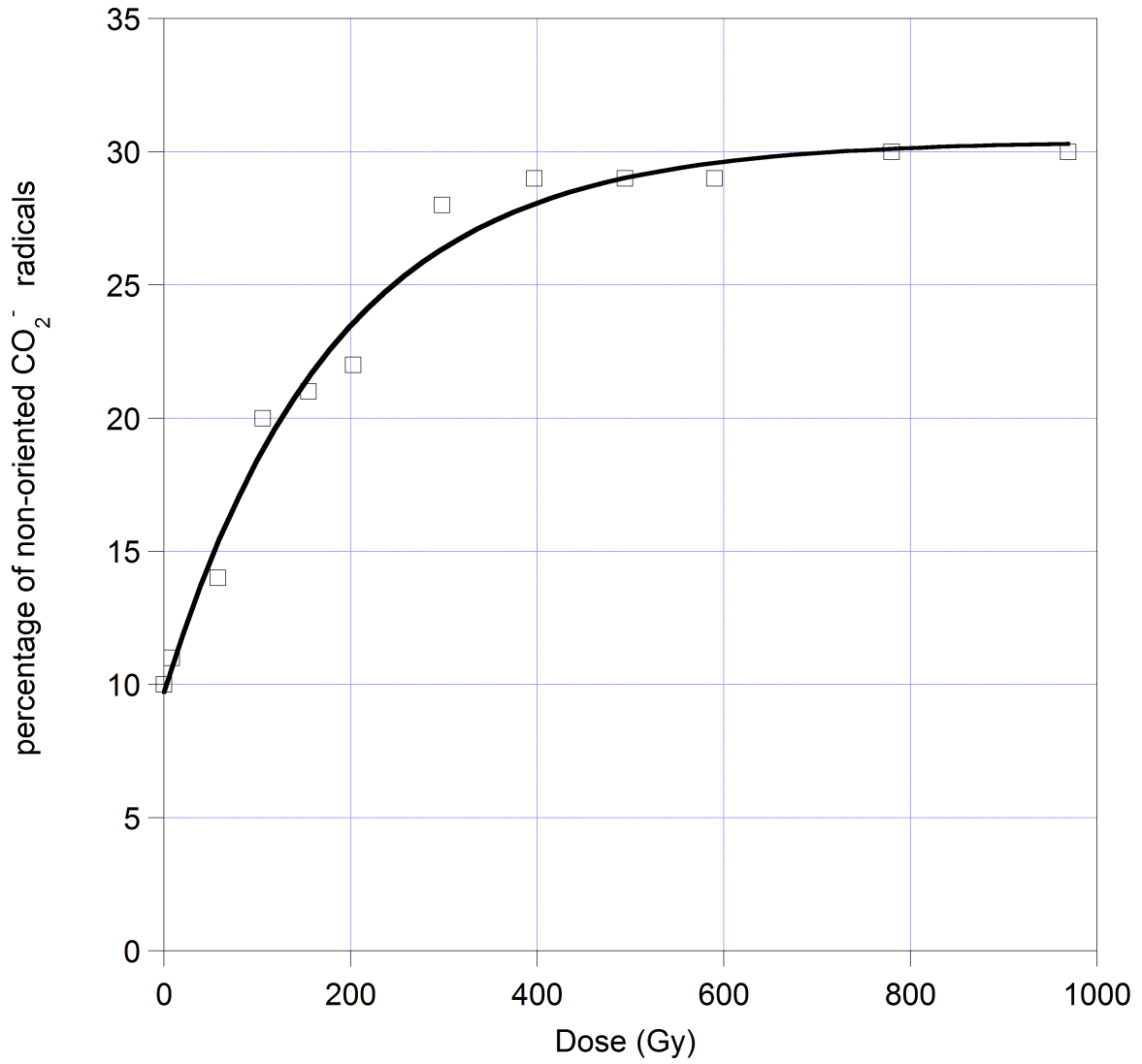


**Extended Data Figure 6 | Stone artefacts from layer 7.** a, c, Single scrapers. b, Double scraper with some edge damage. d, Notch on silicified limestone. e, Single scraper with some edge damage on a Levallois flake. f, Convergent denticulate (Tayac Point). g, Double scraper. h, Déjété scraper. i, Unifacial point. All artefacts are flint unless noted otherwise.



**Extended Data Figure 7 | Dose–response curves of the exponentially fitted thermoluminescence temperature integrals, where the regeneration dose–response curves were shifted along the dose axis to obtain the palaeodoses. The similarity (homothety) of the dose–response**

curves is given by the ratios of the thermoluminescence integrals of the additive and shifted regeneration dose–response curves at the additive dose points. The inset depicts the glow curves and the heating plateau for 300–600 Gy additive  $\beta$ -irradiations.



Extended Data Figure 8 | Estimation and fitting of non-oriented  $\text{CO}_2^-$  radicals (ESR).

Extended Data Table 1 | Lithic data

<b>a</b>	4	5	6	7	Totals
Convergent Scraper	0	3	6	5	14
Déjetés Scraper	0	0	1	4	5
Double Scraper	0	1	3	5	9
Notched	0	5	4	7	16
Other Scrapers	0	0	3	2	5
Retouched Point	0	2	3	1	6
Simple Scraper	2	7	8	10	27
Transverse Scraper	1	0	2	0	3
Truncated-faceted	1	0	1	2	4
Core	1	0	0	1	2
Platform Flake	1	8	17	24	50
Flake Debris	7	22	69	68	166
Shatter	1	1	5	6	13
Totals	14	49	122	135	320

<b>b</b>	4	5	6	7	Totals
Cortical	0	2	3	4	9
Dihedral	4	7	13	13	37
Faceted	0	2	17	13	32
Other	0	0	0	1	1
Plain	6	22	51	48	127
Punctiform	0	1	2	1	4
Totals	10	34	86	80	210

<b>c</b>	4	5	6	7	Totals
Retouch	0	0	1	1	2
Blade	0	0	1	1	2
Levallois	2	14	20	26	62
Normal	8	30	80	79	197
Totals	10	44	102	107	263

**a**, Counts by layer (from the recent excavations) for stone artefact classes. Retouched point corresponds to a Mousterian Point in European Middle Palaeolithic terminology. Platform flakes include complete and proximal flakes. **b**, Platform types. **c**, Blank technology. Normal means that no particular technology could be identified.

Extended Data Table 2 | Dosimetric and thermoluminescence data

A

layer	dosemeter ID	x (m)	x (m)	z (m)	D (μGy a <sup>-1</sup> ) ±
4	7	1000.38	1006.79	97.76	844 24
5	1	1000.24	1007.69	97.37	776 23
5	2	1000.36	1007.07	97.37	918 13
5	3	1000.87	1006.63	97.41	888 120
5	116	1000.87	1006.63	97.41	805 9
5	6	1000.29	1007.60	97.64	962 48
5	9	999.88	1007.74	97.45	951 16
5	507	1000.35	1006.85	97.60	668 22
5	509	999.68	1006.67	97.57	741 32
5	510	1000.36	1006.87	97.36	852 28
5	513	999.68	1006.71	97.36	833 21
5	104	1000.35	1006.85	97.60	749 22
5	109	999.68	1006.67	97.57	752 26
5	110	1000.36	1006.87	97.36	796 86
5	112	999.68	1006.71	97.36	873 64
<b>Layer 5 simple average</b>					<b>826</b>
6	4	1000.33	1007.32	97.18	927 30
6	5	1000.93	1006.70	97.20	906 28
6	8	999.82	1007.53	97.17	889 21
6	35	1000.82	1005.47	97.60	997 55
6	36	1000.24	1005.28	97.53	917 49
6	43	1001.05	1005.53	97.47	1021 83
6	44	1000.32	1005.23	97.14	885 24
6	45	999.79	1005.05	97.22	837 25
6	118	1000.93	1006.70	97.20	834 38
6	514	1000.21	1006.86	97.10	829 43
6	515	999.73	1006.75	97.10	778 37
6	61	1000.51	1005.34	97.34	876 59
6	113	1000.21	1006.86	97.10	891 36
6	114	999.73	1006.75	97.10	802 37
<b>Layer 6 simple average</b>					<b>885</b>
7A	31	1000.40	1006.93	96.94	732 23
7A	32	999.90	1006.80	96.86	973 20
7A	33	999.41	1006.70	96.85	912 58
7A	517	999.47	1006.95	96.76	777 31
7A	519	999.50	1006.83	96.78	789 49
7A	523	999.83	1006.83	96.80	751 22
7A	524	999.75	1006.94	96.81	886 33
7A	46	1001.19	1005.52	97.14	870 11
<b>Layer 7A simple average</b>					<b>836</b>
7B	34	1001.02	1006.64	96.92	754 28
7B	504	1001.35	1006.05	96.99	704 29
7B	516	999.74	1007.03	96.72	691 37
7B	47	1000.94	1005.44	96.99	918 31
7B	48A	1000.47	1004.86	96.59	825 129
7B	49	999.92	1004.72	96.47	907 87
7B	51	999.84	1004.66	96.44	948 29
<b>Layer 7B simple average</b>					<b>821</b>
7C	518	999.65	1006.79	96.40	688 25
7C	520	999.20	1006.71	96.41	660 42
7C	48B	999.94	1004.98	96.23	745 64
<b>Layer 7C simple average</b>					<b>698</b>
<b>all Layer 7 simple average</b>					<b>807</b>

B

Layer	sample	<sup>238</sup> U-series			<sup>232</sup> Th-series		K
		<sup>238</sup> U	<sup>226</sup> Ra	<sup>210</sup> Pb	<sup>228</sup> Ra	<sup>228</sup> Th	
4	JI-27	19.7 ± 5.7	20.0 ± 1.4	15.5 ± 10.9	35.9 ± 2.3	36.0 ± 2.2	877 ± 53
5	JI-23	24.1 ± 3.4	22.7 ± 1.6	21.0 ± 5.7	31.5 ± 2.1	31.3 ± 1.9	875 ± 53
6	JI-28	19.3 ± 3.5	17.9 ± 1.3	17.0 ± 4.7	28.8 ± 1.9	28.6 ± 1.9	762 ± 46
7A	JI-2052	20.8 ± 4.5	19.5 ± 1.5	26.6 ± 8.9	29.6 ± 2.1	29.4 ± 1.8	790 ± 48
7B	JI-1933	30.5 ± 4.2	25.1 ± 1.9	25.4 ± 7.7	26.3 ± 1.9	26.5 ± 1.7	682 ± 42
7C	JI-2295	36.5 ± 4.7	38.6 ± 2.7	34.2 ± 9.2	26.4 ± 1.9	26.6 ± 1.7	680 ± 42

C

Layer	sediment moisture (% dry weight)	number of dosimeters	$\dot{D}_i$ Al <sub>2</sub> O <sub>3</sub> in situ (μGy a <sup>-1</sup> )	$\dot{D}_i$ HpGe dry (μGy a <sup>-1</sup> )	$\dot{D}_i$ HpGe moisture corrected (μGy a <sup>-1</sup> )	difference $\dot{D}_i$ -Al <sub>2</sub> O <sub>3</sub> to moist $\dot{D}_i$ -HpGe (%)
4	9	1	844	1294	1179	-28
5	9	14	826	1263	1157	-29
6	4	14	885	1099	1054	-16
7A	10	8	836	1157	1045	-20
7B	12	7	821	1125	994	-17
7C	10	3	698	1180	1065	-35

D

EVA-LUM	ID	level	X (m)	Y (m)	Z (m)	integral (°C)	palaeo-dose (Gy) ±	S-alpha (μGy/s/10 <sup>3</sup> α/cm <sup>3</sup> ) ±	U (ppm) ±	Th (ppm) ±	K (ppm) ±	$\dot{D}_{int, \gamma}$ (μGy a <sup>-1</sup> ) ±	$\dot{D}_{int, \alpha}$ (μGy a <sup>-1</sup> ) ±	$\dot{D}_{int, \alpha}$ (μGy a <sup>-1</sup> ) ±	$\dot{D}_i$ (μGy a <sup>-1</sup> ) ±	$\dot{D}_{int, ext, \gamma}$ (μGy a <sup>-1</sup> ) ±	$\dot{D}_{int, ext, \alpha}$ (μGy a <sup>-1</sup> ) ±	$\dot{D}_{total}$ (μGy a <sup>-1</sup> ) ±	age (ka) ±
07/15	871	4	1000.01	1007.11	97.92	330-360	307 31	2.8 0.2	0.70 0.11	0.14 0.03	1200 38	810 76	356	202 17	237 18	886 122	1123 123	274 36	
07/16	1144	4	1000.19	1006.44	98.04	350-420	437 52	2.5 0.2	1.25 0.10	0.06 0.02	669 28	802 76	527	237 15	290 17	878 120	1167 121	374 52	
07/17	1013	5	999.78	1007.81	97.41	330-430	574 50	2.0 0.1	5.53 0.23	0.16 0.03	1110 34	805 76	187 13	899 34	1085 36	881 121	1967 126	292 27	
07/18	1343	5	999.50	1006.96	97.36	360-400	343 22	2.8 0.1	0.87 0.09	0.14 0.04	829 33	793 76	435	197 13	240 14	869 119	1109 120	309 35	
07/19	1047	6	999.54	1007.73	97.07	350-410	295 38	2.5 0.2	1.43 0.16	0.19 0.02	581 27	832 76	638	260 23	323 24	908 125	1231 127	240 35	
07/21	1466	6	1000.55	1007.72	97.09	350-410	431 39	3.2 0.1	2.20 0.21	0.17 0.02	1290 44	858 76	122 12	428 31	550 33	934 129	1484 133	290 32	
07/25	1391	6B	999.71	1006.75	97.30	370-430	422 21	1.7 0.1	1.95 0.18	0.11 0.02	644 35	841 76	576	339 26	395 27	917 126	1312 129	322 34	
08/03	1745	6	1000.303	1007.25	96.92	350-400	366 41	2.5 0.1	0.99 0.10	0.12 0.04	870 39	854 76	435	217 14	260 15	930 128	1190 129	307 42	
07/28a	1515	7A	1000.351	1007.83	96.98	360-410	529 53	3.2 0.1	2.79 0.11	0.07 0.01	334 23	765 70	1539	435 16	588 18	835 115	1423 116	372 43	
07/28b	dito	7A	dito	dito	dito	350-420	561 53	3.2 0.2	3.01 0.10	0.05 0.01	320 22	765 70	1619	465 15	626 18	835 115	1461 116	384 42	
08/05	1588	7A	999.93	1007.76	96.78	350-365	344 19	2.6 0.2	1.22 0.10	0.08 0.04	681 23	806 70	556	234 15	289 16	876 121	1165 122	295 32	
08/06	1816	7A	1000.15	1007.42	96.84	360-390	340 26	1.4 0.1	1.07 0.08	0.10 0.03	374 13	811 70	262	189 11	214 12	881 122	1095 122	310 38	
08/07	1835	7A	999.52	1007.26	96.83	330-350	423 25	1.4 0.1	1.96 0.12	0.12 0.03	899 29	811 70	485	361 18	409 19	881 122	1290 123	328 33	
08/08	1837	7A	1000.02	1007.26	96.82	350-420	374 30	3.2 0.9	1.08 0.07	0.10 0.03	335 15	811 70	60 18	187 10	247 20	881 122	1128 123	332 41	
08/12	1924	7B	1000.45	1007.07	96.68	350-400	442 53	2.7 0.3	2.08 0.10	0.24 0.05	937 30	788 70	99 12	384 15	484 19	858 118	1342 120	329 44	

a, Layers, locations and  $\gamma$ -dose-rates for individual dosimeters and average context dose-rates. b, Total activities from HpGe  $\gamma$ -ray spectrometry (Bq kg<sup>-1</sup> at 2 $\sigma$ ) on dry samples of all sediment particles smaller than 4 cm, based on an estimated 95% SiO<sub>2</sub> and 5% BaSO<sub>4</sub> composition. For the <sup>238</sup>U-series the  $\gamma$ -lines from <sup>234</sup>Th were used for <sup>238</sup>U; for <sup>226</sup>Ra from <sup>214</sup>Pb and <sup>214</sup>Bi; for <sup>210</sup>Pb from <sup>210</sup>Pb. For the <sup>232</sup>Th-series the estimates for <sup>228</sup>Ra are based on <sup>228</sup>Ac and for <sup>228</sup>Th on <sup>212</sup>Pb, <sup>212</sup>Bi and <sup>208</sup>Tl. c, Comparison of  $\gamma$ -dose-rates obtained with *in situ*  $\alpha$ -Al<sub>2</sub>O<sub>3</sub>:C dosimeters and HpGe  $\gamma$ -ray spectrometry on dry sediment, with the latter corrected for measured moisture content. d, Thermoluminescence sample identifiers, provenience and analytical results for heated flint samples from Jebel Irhoud (a, b, indicate independent subsamples from a single artefact, for which a weighted average age was calculated). The effective external  $\gamma$ -dose-rates account for the shape and weight of samples<sup>65</sup>. All uncertainties at 1 $\sigma$ , with calculations following ref. 32.

Extended Data Table 3 | ESR age calculation

<b>Enamel</b>	
Dose (Gy)	326 ± 16
U (ppm)	0.07 ± 0.04
Alpha Efficiency	0.13 ± 0.02
Thickness (µm)	1000 ± 200
<b>Dentine</b>	
U (ppm)	3.76 ± 0.43
$^{234}\text{U}/^{238}\text{U}$	1.5287 ± 0.0088
$^{230}\text{Th}/^{234}\text{U}$	0.7186 ± 0.0114
Water (%)	5 ± 5
<b>Sediment</b>	
U (ppm)	2.37 ± 0.67
Th (ppm)	6.77 ± 0.47
K (%)	2.32 ± 0.22
Water (%)	11 ± 5
<b>External Sediment Dose rates</b>	
alpha (µGy a <sup>-1</sup> )	6 ± 1
beta (µGy a <sup>-1</sup> )	276 ± 51
gamma (µGy a <sup>-1</sup> )	751 ± 100
cosmic (µGy a <sup>-1</sup> )	70 ± 7
total (µGy a <sup>-1</sup> )	1102 ± 112
<b>EARLY U-uptake model</b>	
internal dose rate (µGy a <sup>-1</sup> )	33 ± 20
beta dose rate, dentine (µGy a <sup>-1</sup> )	74 ± 13
total dose rate (µGy a <sup>-1</sup> )	1209 ± 115
Age (ka)	269 ± 28
<b>Linear U-uptake model</b>	
internal dose rate (µGy a <sup>-1</sup> )	14 ± 9
beta dose rate, dentine (µGy a <sup>-1</sup> )	32 ± 6
total dose rate (µGy a <sup>-1</sup> )	1148 ± 113
Age (ka)	283 ± 31
<b>Combined U-series ESR model</b>	
internal dose rate (µGy a <sup>-1</sup> )	18 ± 11
beta dose rate, dentine (µGy a <sup>-1</sup> )	39 ± 9
p (beta)	-0.27 ± 0.14
total dose rate (µGy a <sup>-1</sup> )	1159 ± 113
Age (ka)	281+37/-29
<b>Closed System U-series ESR model</b>	
Dose from U in enamel and dentine (Gy)	10.6 ± 0.3
Age (ka)	286 ± 32

For comparison with previously published ESR results, age calculations were also carried out for the parametric early and linear U-uptake models.